

This is a non-peer-reviewed preprint submitted to EarthArXiv.

This manuscript has been submitted for publication in *Geophysics*. Please note the manuscript has yet to be reviewed and formally accepted for publication. Subsequent versions of this manuscript may have slightly different content. If accepted, the final version of this manuscript will be available via the 'Peer-reviewed Publication DOI' link on the right-hand side of this webpage. Please feel free to contact any of the authors; we welcome feedback.

# Unsupervised data selection for focused time-lapse inversion in electrical resistivity tomography monitoring

Thomas Hermans<sup>1</sup>, Arne Maene<sup>1</sup>, Corentin Caudron<sup>2</sup>, Lore Vanhooren<sup>1,2</sup>

<sup>1</sup>Department of Geology, Ghent University, 9000 Gent, Belgium

<sup>2</sup>G-TIME Laboratory, Université Libre de Bruxelles (ULB), Brussels, Belgium ABSTRACT Time-lapse electrical resistivity tomography (TLERT) is a popular technique to monitor subsurface processes. Inversions and interpretation often remain challenging because of noisy data and the superposition of several processes influencing the results. To improve TLERT imaging, we apply clustering of data time series prior to the inversion process. We invert only for a subset of data points displaying some interesting temporal variations. This approach allows to reduce data misfit within the data subset and successfully isolate the main processes from other taking place along the measuring profile. This opens new perspectives for the processing of TLERT data and the monitoring of subsurface processes.

## **KEYWORDS**

Electrical Resistivity Tomography, Clustering, time-lapse inversion, data misfit, long-term monitoring

## HIGHLIGHTS

- Unsupervised clustering is used to select subsets of time-lapse ERT monitoring data showing interesting temporal trends
- 2. Selected subsets are inverted separately to focus imaging and identify the origin of the signal
- 3. Results show the approach is efficient to remove other variations and reduce data misfit

#### INTRODUCTION

Long-term monitoring of subsurface processes using time-lapse electrical resistivity tomography (TLERT) has recently gained popularity (Dimech et al., 2022; Hermans et al., 2023). Long-term monitoring poses several challenges for inversion: regularization strongly impacts the recovered resistivity (e.g., Dimech et al., 2022); varying noise level can produce artifacts (Lesparre et al., 2017); interpretation is complex since long-term changes are impacted by several factors, such as salinity, saturation and temperature (Singha et al., 2015) often superimposed or affecting differently parts of the profile (e.g. Hermans et al., 2012).

Clustering approaches on TLERT inverted time series were suggested to identify zones with similar trends and disentangle subsurface processes. Delforge et al. (2021) tested several clustering approaches after normalization and dimension reduction to identify various trends in karst infiltration processes. Gonzalez and Misra (2022) applied k-means clustering combined with dynamic time wrapping to image carbon storage, and optimized the number of clusters.

Cozzolino et al. (2020) obtained consistent resistivity distributions while selecting only a data subset selected based on the location of data points within a horizontal window. It was only applied to static surveys. Optimizing electrode configurations has been proposed (Furman et al., 2013; Uhlemann et al., 2018), but relies on knowing the location of expected resistivity changes.

In this contribution, we apply clustering on TLERT resistance time series rather than inverted resistivity sections, allowing the selection of data points with an interesting temporal behaviour. The spatial origin of this signal is identified and disentangled from other processes taking place along the profile. It improves the data misfit within the selected cluster, leading to improved inversion results within the zone of interest, crucial for quantitative interpretation. We demonstrate our approach on TLERT collected on an active hydrothermal system. To our knowledge, this is the first time clustering of resistance time series is applied prior to inversion, opening new perspectives for the processing and quantitative interpretation of long-term TLERT data sets.

#### **METHODOLOGY**

#### **Subset selection**

We first filter outliers by calculating the distance between percentiles 15 and 85 for each resistance time series. Isolated measurements falling outside 1.5 this range (see Figure S1E) are replaced by the linear interpolation from the previous and next timestep while points for which these time steps are also identified as potential outliers are kept, as they are related to consistent and interesting features. The time series are normalized to reduce the impact of the amplitude on clustering results. The minmax normalization rescales time series between 0 and 1

$$R_{norm}(t) = \frac{R(t) - \min(R(t))}{\max(R(t)) - \min(R(t))} \tag{1}$$

where R(t) and  $R_{norm}(t)$  are the measured and normalized resistance time series respectively, and min and max the minimum and maximum value of the time series. We also use the zero-mean unit-variance distribution normalization which is not bounded:

$$R_{norm}(t) = \frac{R(t) - \mu_R}{\sigma_R} \tag{2}$$

where  $\mu_R$  and  $\sigma_R$  are the mean and standard deviation of the time series respectively. Clustering is applied separately on the two normalized resistance series, and then merged before inversion. Because of normalization, working with apparent resistivity instead of resistance yields similar results.

Since TLERT data sets contain a lot of redundancy, in time and space, we reduce the dimension of the data before clustering using multi-dimensional scaling (MDS). The pairwise Euclidean distance between normalized time series is calculated and mapped in a lower dimensional space. MDS is preferred over principal component analysis for its ability to capture non-linearity (Lopez-Alvis, 2019) which is confirmed by the explained variance retained in the 3 first dimensions (> 95 %).

Finally, k-means clustering is applied in the MDS space. The number of clusters is selected according to the silhouette index (Kaufman and Rousseuw, 1990). The clusters are analyzed to identify those containing interesting temporal trends. The other clusters still contain temporally variable quadrupoles, but with other temporal features.

# **Inversion**

We used the time-constrained inversion (e.g. Miller et al., 2008) to reduce artefacts of inversion by minimizing the difference with a reference model. The objective function is expressed as (Hermans and Paepen, 2020):

$$\phi(\mathbf{m}) = \|\mathbf{W_d}(\mathbf{d} - f(\mathbf{m})\|_2 + \lambda(\|\mathbf{W_m}(\mathbf{m} - \mathbf{m_0})\|_2 + \alpha\|\mathbf{m} - \mathbf{m_0}\|_2)$$
(3)

where m is the natural logarithm of the resistivity, d is the natural logarithm of the resistance, f is the forward model,  $\mathbf{W_d}$  is the data weighting matrix,  $\mathbf{W_m}$  is the roughness matrix, and  $m_0$  is the reference model.  $\lambda$  is the regularization factor, balancing between the data misfit and model misfit terms, while  $\alpha$  is the closeness factor for the reference model. The reference model is the inverted model obtained for the first full data set of the time series, using the same objective function but with no reference model. This ensures that inversions with the data subset remain consistent in terms of absolute resistivity values, including in non-sensitive parts of the section.

Inversions are performed using CRTomo (Kemna, 2000), which uses a Gauss-Newton approach for minimizing the objective function and a line search to optimize  $\lambda$ . The inversion stops when the global error weighted root-mean-square error  $\epsilon_{RMS}$  is equal to 1, reaching its expected error level (Thibaut et al., 2021):

$$\epsilon_{RMS} = \sqrt{\frac{1}{N} \sum_{i=1}^{N} \frac{\left(d_i - f_i(\mathbf{m})\right)^2}{e_i^2}} \tag{4}$$

where *N* is the number of data points. A robust data constraint is used to limit the impact of outliers (Kemna, 2000). When applied to a subset, this criterion ensures the subset is fitted to its error level. For the full data set, this criterion is only valid globally, which can lead to over-/underfitting in individual subsets.

## RESULTS

## Field data

The data set was collected in Iceland on a hydrothermal system, located close to the Gunnhuver hot spring (Figure S2). A 72-electrode 355 m-long ERT profile was installed in a zone containing several hydrothermal features and inactive portions (Vanhooren et al., 2025a). Daily data were automatically collected using a Syscal Pro Switch (Iris Instruments) and a multigradient protocol from November 2022 for 1 year. Until June 2023, only limited variations are observed (Figure S1). In June 2023, some quadrupoles start to display strong positive or negative anomalies, with much larger amplitude, culminating in two peaks (Figures S1, 1D, 1E, 1J, 1K), while other do not show any significant

variations (Figures S1, 1F, 1L). Since this period corresponds with a strong volcanic activity in the Reykjanes peninsula, we want to isolate the quadrupoles affected by these peaks and understand their origin.

#### **Subset selection**

K-means clustering is applied on the MDS maps obtained with the two normalizations and an optimum number of 6 clusters (Figure 1). Both normalizations recover similar patterns in the data. Selected clusters contain data points displaying a clear trend in which positive or negative peaks are observed. They are mostly located in the right part of the pseudosection. The data points with negative peaks are mostly very shallow, while the points with positive peaks are found deeper.

We also observe isolated points in the pseudosections, and points with different temporal trends. This is a consequence of k-means clustering, which classifies points based on their distance (in MDS space) to the cluster centre, inducing uncertainty at the boundaries. We therefore combine the results of both normalizations, and keep only the datapoints selected for both approaches. The selected subset contains 625 quadrupoles out of the 1624 initial ones.

# Inversion

The full data set of June 1 (Figure S3) is used as a reference for the time-constrained inversion of a profile every 10 days until the end of October and shown for 5 selected dates (Figure 2). The closeness factor  $\alpha$  is fixed to 0.3. A linear resistance error model with a relative error of 1% and absolute error of 0.0005 Ohm was deduced from reciprocal data (Vanhooren et al., 2025a, 2025b). The results for each time step  $\rho_i$  are displayed as percentage change in resistivity  $\Delta \rho$  in comparison to the inversion results of June 1 obtained through the time-constrained inversion ( $\rho_0$ ):

$$\Delta \rho = \frac{\rho_i - \rho_0}{\rho_0} \times 100 \tag{5}$$

With both data sets, the image is dominated by strong changes in resistivity up to more than 150 % between 150 and 300 m. The changes are negative in the shallow part and positive in the deeper part. They appear around June 20, reach a peak around July 10, evolve towards a local minimum on July 30, rise again until August 30, then slowly decrease to the initial level at the end of October. This zone has a higher elevation on the profile and no hydrothermal alteration (Vanhooren et al., 2025a).

Inversions with the full data set also contain resistivity variations in the first 150 m, which is hydrothermally active. Their amplitude is limited between -30 and +50 %. Resistivity changes in the very shallow layers are also present, typical of the hydrothermal activity, and are observed all year long. Since they are not part of the selected clusters, these variations are absent of inversions with the selected clusters in which only anomalies related to the peaks are observed. The cumulative sensitivity (Figures 2F and 2L) indicates that the selected data subset is less sensitive to this part of the profile and therefore does not resolve corresponding resistivity changes, not related to the identified peaks.

The amplitude and spatial extent of the resistivity changes are larger for the selected clusters, especially at the peaks. The cluster selection successfully identifies the interesting trend and leads to more focus imaging. It indicates that the presence of the peak is limited to a specific area of the profile, not visibly active. This cannot be unequivocally derived from the full data set which also displays resistivity changes in hydrothermally active zones.

#### Data misfit

The difference in recovered resistivity variations is intimately linked to the inversion. The convergence criterion is related to the solution reaching an error corresponding to its estimated noise level (e.g., Thibaut et al., 2021), ensuring the data set is not globally over-/underfitted. However, this criterion averages over the whole data set, points having a better or lower fit compensate each other. The  $\epsilon_{RMS}$  within the selected subset is lower when only the subset is inverted, compared to inversion with the full data set (Table S1, Figure 3). The average value across timesteps decreases from 3.05 to 2.64 and from 1.19 to 1.04 when calculated in resistance and log resistance scales respectively. The differences are most significant during the peaks. On August 10 for instance, the log  $\epsilon_{RMS}$  drops from 1.58 to 1.1 when inverting only the subset. The inversion of the full data set thus leads to underfitting within the selected clusters, and a worse fit of the peaks, which must be compensated by an overfitting of quadrupoles in other areas.

The improved fitting is confirmed by the absolute and relative misfit within the selected clusters (Figure 3). The relative error decreases for deep points, where the measured resistance is low, and for the shallowest data points characterized by negative peaks. In contrast, the absolute error decreases more

significantly in the upper part of the pseudosection where resistance is higher. This likely explains why the absolute resistivity changes are larger when inverting only the selected subset (Figure 2).

The increase in resistivity at depth is likely related to gas trapping below a capping layer, a phenomenon used to explain hydrothermal eruptions (Christenson et al., 2010). The decrease of resistivity in the surficial zone would be rather related to a temperature increase linked to a higher heat flux. In active zones, discharge pathways for gas exist, so that resistivity changes are not affected. This hypothesis should be validated by additional data and modelling, but this falls out of the scope of this paper.

# **CONCLUSION**

Disentangling resistivity changes in TLERT is difficult owing to multiple factors affecting resistivity. We propose to select a data subset based on the temporal behaviour of measured resistances. The time series are normalized, projected in a lower dimensional space and clustered. Clusters showing interesting temporal behaviour are selected for inversion. The methodology is fully unsupervised and automated. Only the selection of the clusters requires expert input.

The qualitative evolution of resistivity in the zone sensitive to the selected clusters is not affected by the selection. The resistivity variations having other trends are successfully removed, allowing to focus the interpretation on the process of interest only. The data misfit for the selected clusters is smaller when the subset is inverted alone, leading to a local improvement in the recovered resistivity changes, making more quantitative interpretation possible.

A potential drawback of subset inversion is that non-sensitive zones could negatively impact the recovered resistivity changes. This should be further investigated through in-depth numerical studies, ideally involving hydrogeophysical coupled modeling.

The proposed methodology has the potential to be broadly applied in TLERT when several processes affect the resistivity. Therefore, the inversion of selected clusters should not replace inversion of the full data sets which image all processes taking place simultaneously, but should rather be applied after identification of interesting signals, to refine imaging. Future works should focus on more advanced clustering to avoid the presence of outliers within the selected clusters, or of missing interesting points, for example by adding some spatial constraints during clustering. Another improvement would be to

apply the convergence criterion per cluster, ensuring each cluster is fitted to its estimated noise level.

This would adequately retain all data points, and thus full sensitivity, while avoiding over-/underfitting.

#### REFERENCES

Christenson, B. W., A. G. Reyes, R. Young, A. Moebis, S. Sherburn, J. Cole-Baker, and K. Britten, 2010, Cyclic processes and factors leading to phreatic eruption events: insights from the 25 September 2007 eruption through Ruapehu Crater Lake, New Zealand: Journal of Volcanology and Geothermal Research, 191, 15-32.

Cozzolino, M., P. Mauriello, and D. Patella, 2020, An Extension of the Data-Adaptive Probability-Based Electrical Resistivity Tomography Inversion Method (E-PERTI): Geosciences, **10**, no. 10, 380. <a href="https://doi.org/10.3390/geosciences10100380">https://doi.org/10.3390/geosciences10100380</a>

Delforge, D., A. Watlet, O. Kaufmann, M. Van Camp, and M. Vanclooster, 2021, Time-series clustering approaches for subsurface zonation and hydrofacies detection using a real time-lapse electrical resistivity dataset: Journal of Applied Geophysics, **184**, 104203.

https://doi.org/10.1016/j.jappgeo.2020.104203

Dimech, A., L. Cheng, M. Chouteau, J. Chambers, S. Uhlemann, P. Wilkinson, P. Meldrum, B. Mary, G. Fabien-Ouellet, and A. Isabelle, 2022, A Review on Applications of Time-Lapse Electrical Resistivity Tomography Over the Last 30 Years: Perspectives for Mining Waste Monitoring: Surveys in Geophysics, 43, no. 6, 1699–1759. <a href="https://doi.org/10.1007/s10712-022-09731-2">https://doi.org/10.1007/s10712-022-09731-2</a>

Gonzalez, K., and S. Misra, 2022, Time-Lapse Monitoring of the Dynamic Geological Carbon Storage Using Unsupervised Spatiotemporal Clustering: SSRN Electronic Journal,

https://doi.org/10.2139/ssrn.4156583

Furman, A., T. P. A. Ferré and A.W. Warrick, 2003, A Sensitivity Analysis of Electrical Resistivity Tomography Array Types Using Analytical Element Modeling: Vadose Zone Journal, **2**, no. 3, 416–423. <a href="https://doi.org/10.2136/vzj2003.4160">https://doi.org/10.2136/vzj2003.4160</a>

Hermans, T., A. Vandenbohede, L. Lebbe, and F. Nguyen, 2012, A shallow geothermal experiment in a sandy aquifer monitored using electric resistivity tomography: Geophysics, 77, no. 1, B11–B21. https://doi.org/10.1190/geo2011-0199.1 Hermans, T., and M. Paepen, 2020, Combined Inversion of Land and Marine Electrical Resistivity Tomography for Submarine Groundwater Discharge and Saltwater Intrusion Characterization: Geophysical Research Letters, 47, no. 3, e2019GL085877. <a href="https://doi.org/10.1029/2019GL085877">https://doi.org/10.1029/2019GL085877</a> Hermans, T., P. Goderniaux, D. Jougnot, J.H. Fleckenstein, P. Brunner, F. Nguyen, et al., 2023, Advancing measurements and representations of subsurface heterogeneity and dynamic processes: towards 4D hydrogeology: Hydrology and Earth System Sciences, 27, no. 1, 255–287. <a href="https://doi.org/10.5194/hess-27-255-2023">https://doi.org/10.5194/hess-27-255-2023</a>

https://doi.org/10.5194/hess-27-255-2023

Kaufman L, and P.J Rousseuw, 1990, Finding groups in data: an introduction to cluster analysis: Wiley-Interscience. 10.2307/25321 78.

Kemna, A., 2000, Tomographic Inversion of Complex Resistivity-Theory and Application: PhD thesis, Ruhr-Universität, Bochum, Germany.

Lesparre, N., F. Nguyen, A. Kemna, T. Robert, T. Hermans, M. Daoudi, and A. Flores-Orozco, 2017, A new approach for time-lapse data weighting in electrical resistivity tomography: Geophysics, **82**, no. 6, E325–E333. <a href="https://doi.org/10.1190/geo2017-0024.1">https://doi.org/10.1190/geo2017-0024.1</a>

Lopez-Alvis, J., T. Hermans, and F. Nguyen, 2019, A cross-validation framework to extract data features for reducing structural uncertainty in subsurface heterogeneity: Advances in Water Resources, 133, 103427.

Miller, C. R., P.S. Routh, T.R. Brosten, and J.P. McNamara, 2008, Application of time-lapse ERT imaging to watershed characterization: Geophysics, **73**, no. 3, G7-G17.

Singha, K., F. D. Day-Lewis, T. Johnson, and L. Slater, 2015, Advances in interpretation of subsurface processes with time-lapse electrical imaging: Hydrological Processes, **29**, no. 6, 1549–1576.

Thibaut, R., T. Kremer, A. Royen, B. Kim Ngun, F. Nguyen, and T. Hermans, 2021, A new workflow to incorporate prior information in minimum gradient support (MGS) inversion of electrical resistivity and induced polarization data: Journal of Applied Geophysics, **187**, 104286.

# https://doi.org/10.1016/j.jappgeo.2021.104286

Uhlemann, S., P. B. Wilkinson, H. Maurer, F.M. Wagner, T.C. Johnson and J.E. Chambers, 2018, Optimized survey design for electrical resistivity tomography: combined optimization of measurement configuration and electrode placement: Geophysical Journal International, 214, no. 1,

108–121. <a href="https://doi.org/10.1093/gji/ggy128">https://doi.org/10.1093/gji/ggy128</a> Vanhooren, L., E. Vrancken, W. Dekoninck, A. Flores-Orozco, O. Fontaine, B. Bergsson, K. Jónsdóttir, C. Caudron, and T. Hermans, 2025a, Subsurface hydrothermal alteration mapping in the Reykjanes Geothermal area using a combined geoelectrical approach: in press, Volcanica. <a href="https://doi.org/10.31223/X51F1K">https://doi.org/10.31223/X51F1K</a>

Vanhooren, L., W. Deleersnyder, W. Dekoninck, A. Flores Orozco, F. Nguyen, C. Caudron and T. Hermans, 2025b, Field evidence for non-linear IP effects in a volcanic hydrothermal system using reciprocal data: *EarthArxiv*, <a href="https://doi.org/10.31223/X50T7B">https://doi.org/10.31223/X50T7B</a>.

#### FIGURE CAPTIONS

- **Figure 1**. Clustering results for the min-max normalization (left) and the 0-mean unit-variance normalization (right). Clusters in the 3 dimension MDS space (A and G), Silhouette index indicating the optimum number of clusters (B and H), pseudosection with spatial distribution of the clusters (C and I), resistance series in the selected clusters (D, E, J and K) and one unselected cluster (F, L).
- **Figure 2**. Inversion results with the full data set (left) and the selected subset (right) on June 20 (A and G), July 10 (B and H), July 30 (C and I), August 30 (D and J), October 30 (E and K) and normalized cumulative sensitivity (F and L).
- **Figure 3**. Data misfit for the inversion of August 30 for the point within the selected cluster for the full (left) and selected data sets (right) expressed in relative error (A and C) and absolute error (B and D).

## **FIGURES**

# Figure 1

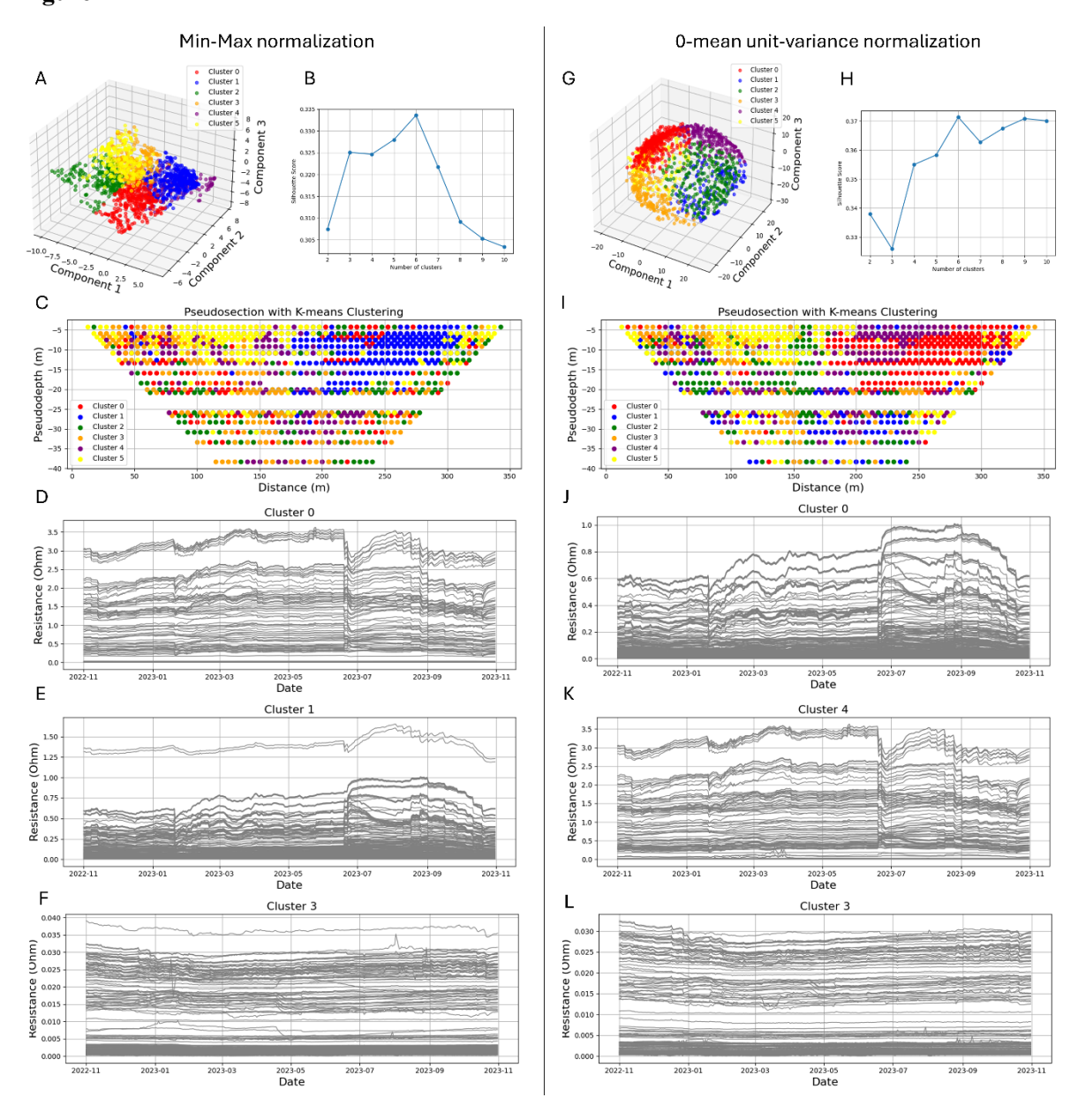


Figure 1. Clustering results for the min-max normalization (left) and the 0-mean unit-variance normalization (right). Clusters in the 3 dimension MDS space (A and G), Silhouette index indicating the optimum number of clusters (B and H), pseudosection with spatial distribution of the clusters (C and I), resistance series in the selected clusters (D, E, J and K) and one unselected cluster (F, L).

# Figure 2

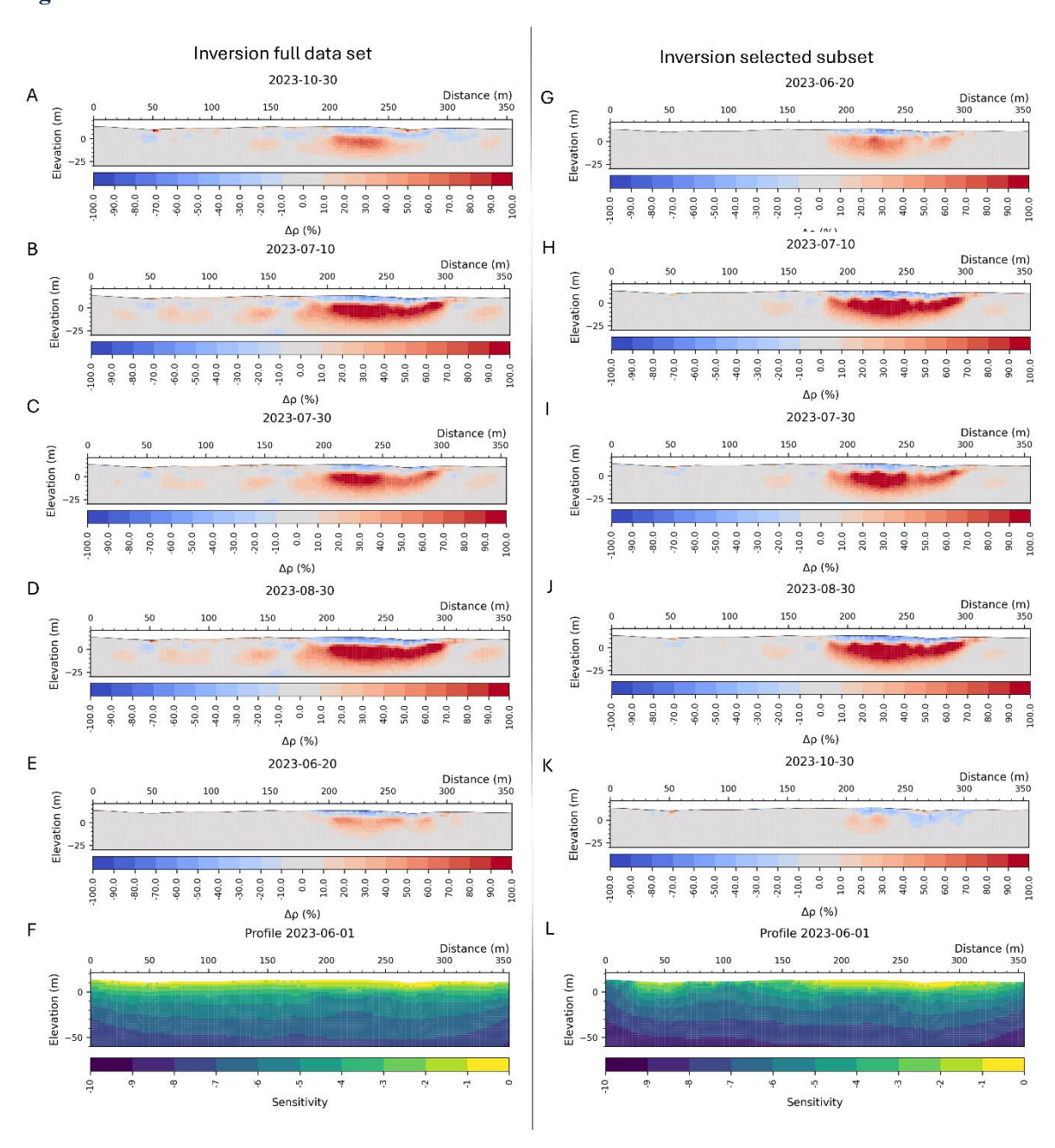


Figure 2. Inversion results with the full data set (left) and the selected subset (right) on June 20 (A and G), July 10 (B and H), July 30 (C and I), August 30 (D and J), October 30 (E and K) and normalized cumulative sensitivity (F and L).

# Figure 3

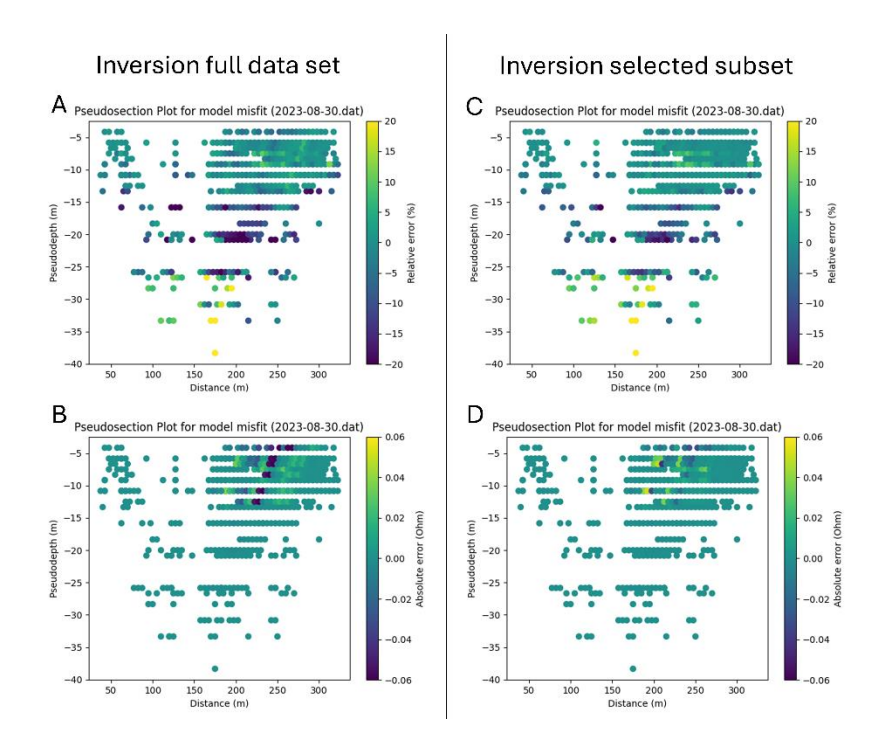


Figure 3. Data misfit for the inversion of August 30 with the full (left) in selected data sets (right) expressed in relative error (A and C) and absolute error

# SUPPLEMENTAL FILES

# **TABLE**

Table S1. Data misfit in the selected clusters for individual time steps in resistance scale and logarithmic scale

DATE	FULL	FULL INVERSION	SUBSET	SUBSET
	INVERSION	LOG SCALE	INVERSION	INVERSION
				LOGSCALE
01/06/2023	2.715	0.904	2.156	0.891
10/06/2023	2.663	1.108	3.339	1.468
20/06/2023	2.147	0.683	1.877	0.832
30/06/2023	2.899	0.785	2.647	1.131
10/07/2023	2.982	0.875	2.63	0.847
20/07/2023	3.265	1.443	2.767	1.108
30/07/2023	3.255	1.477	2.766	0.915
10/08/2023	3.171	1.577	2.825	1.104
20/08/2023	3.022	1.274	2.776	1.473
30/08/2023	3.185	1.267	2.679	0.851
10/09/2023	3.220	1.073	2.715	0.866
20/09/2023	3.155	0.988	2.750	0.774
30/09/2023	3.343	1.257	2.757	0.864
10/10/2023	2.269	0.936	2.649	0.937
20/10/2023	3.833	1.760	2.669	1.242
30/10/2023	3.692	1.701	2.295	1.354
Average	3.05	1.19	2.64	1.05

## **FIGURES**

# Figure S1

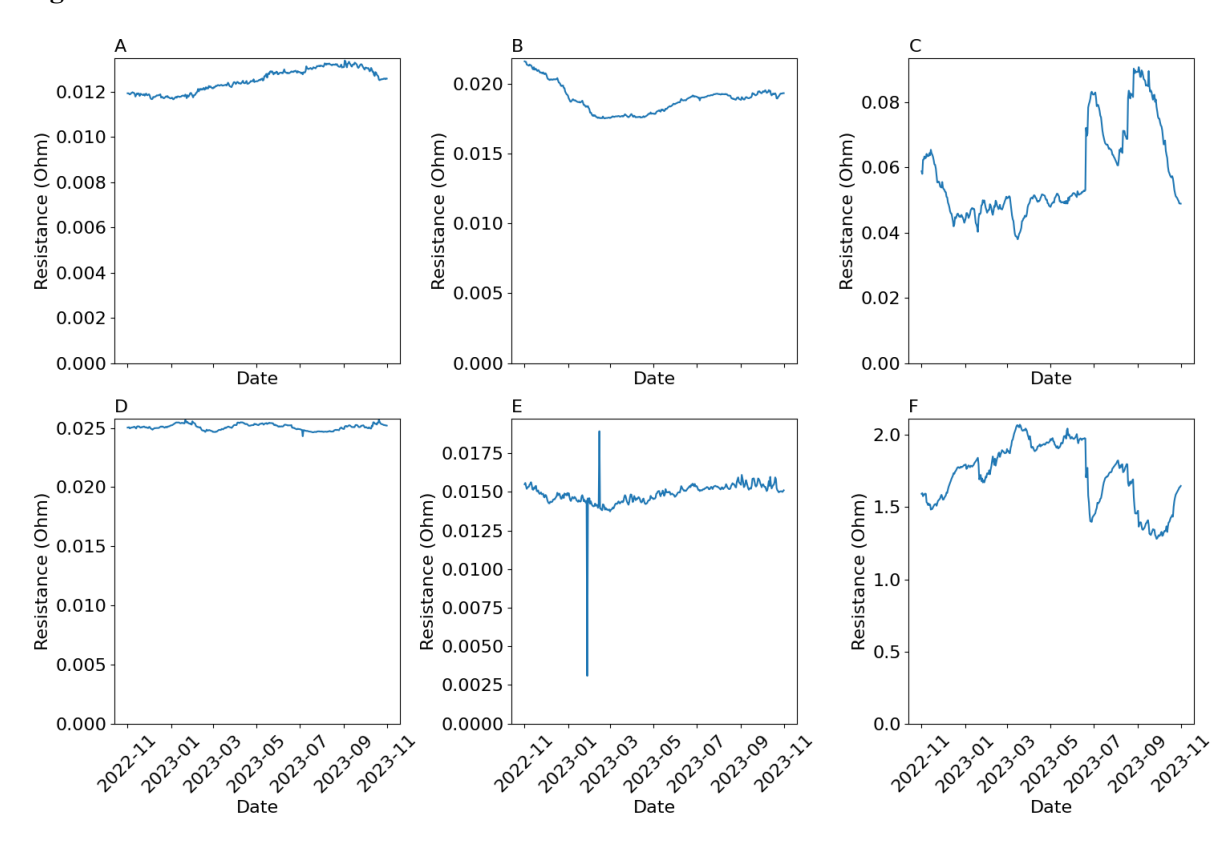


Figure S1: Example of time series contained in the data set. Some data sets show seasonal (A) or long-term (B) trends or some punctual anomalies (D). Some data sets show the clear presence of outliers at specific dates (E). Some data sets show event-related anomalies occurring at specific time (C and F) that are of interest in this study.

Figure S2

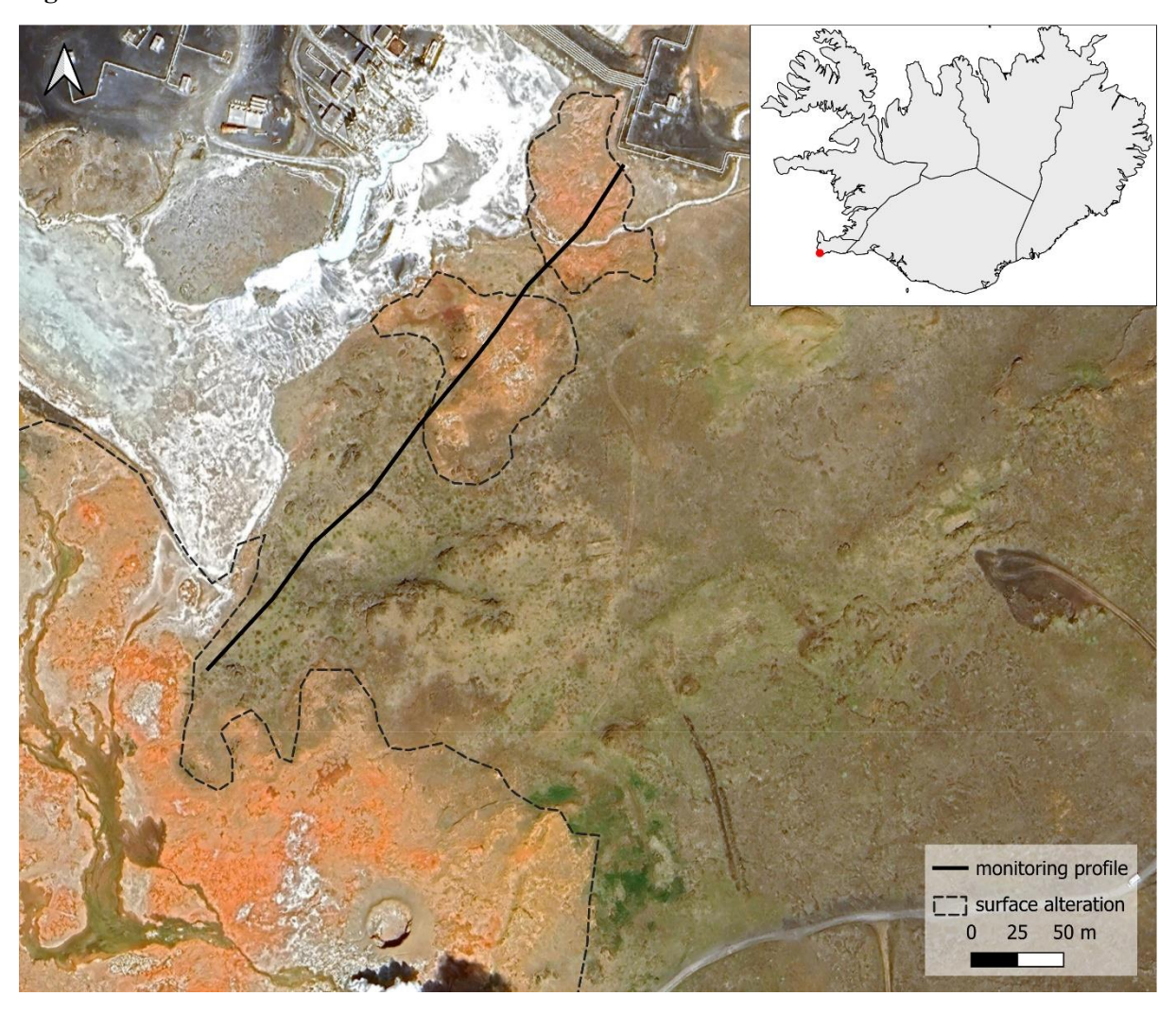


Figure S2: Localization of the study site. Electrode 1 (0 m) is located in the northern part of the site.

# Figure S3

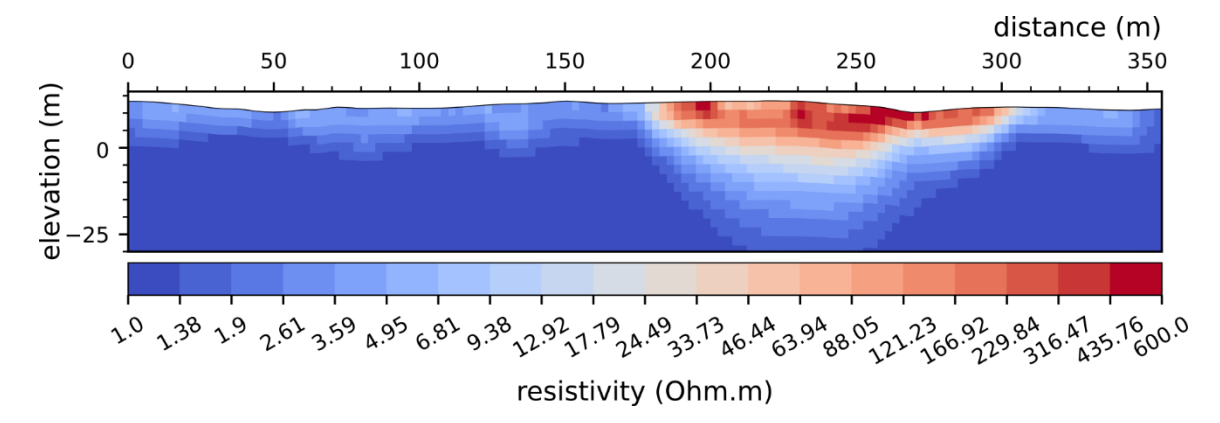


Figure S3: Inverted resistivity of the background profile (June 1st, 2023) used as a reference for the time-constrained inversions